Experimental Thermal and Fluid Science 82 (2017) 58–74

Contents lists available at ScienceDirect

Experimental Thermal and Fluid Science

journal homepage: www.elsevier.com/locate/etfs

Flow around an articulated lorry model

Kin Hing Lo *, Konstantinos Kontis

Division of Aerospace Sciences, School of Engineering, University of Glasgow, University Avenue, Glasgow G12 8QQ, United Kingdom

ARTICLE INFO

Article history:
Received 7 June 2016
Received in revised form 18 September 2016
Accepted 3 November 2016
Available online 4 November 2016

Keywords:
Articulated vehicles
Bluff bodies
Road vehicle aerodynamics
Square back vehicles
Wake flow
Wind tunnel tests

ABSTRACT

An experimental study has been conducted to investigate both the time-averaged and instantaneous flow pattern over a scale articulated vehicle model for understanding the flow physics of tractor-trailer vehicles. Fully turbulent flow was used in the study and smoke visualisation, surface oil flow visualisation and two-component particle image velocimetry were employed for flow diagnostics. Results obtained from the time-averaged and instantaneous flow fields show different flow pattern in the wake region downstream of the rear end of the trailer model. In the time-averaged flow field, a single counter-clockwise rotating vortex is presented in the wake region due to the coil-up of the lower shear layer. The instantaneous flow pattern shows that two wake vortices are presented in the wake region downstream of the trailer model. Moreover, the interactions between the wake vortex and the upper shear layer lead to the formation of the streamwise vortices within the shear layer. These streamwise vortices grow and propagate downstream which lead to the occurrence of vortex shedding in the upper shear layer downstream of the trailer model.

1. Introduction

Heavy Goods Vehicles (HGVs) play an important role in daily domestic goods transportation within the United Kingdom. According to the information shown in the report "Transport Statistics Great Britain 2015" [1], published by the Department of Transport of the United Kingdom Government, approximately 73.5% of domestic freight was transported by HGVs in 2014. In addition, about 15.5 million tonnes of greenhouse gas emissions came from HGVs. Due to the considerably poor aerodynamics efficiency of most HGVs, significant amount of fuel is consumed by HGVs to overcome the aerodynamics drag acting on the vehicles during high-speed operation. Altaf et al. [2] concluded that as much as 65% of fuel is consumed to overcome the aerodynamic drag encountered by buses and HGVs in long-haul journeys. Similarly, Bradley [3] indicated that the aerodynamic drag contributes approximately 21% of energy loss when a 36-tonne heavy goods vehicle is travelling at 105 km/h. Hsu and Davis [4] deduced that an annual fuel cost saving of US$ 10,000 could be achieved if the aerodynamic drag acting on a heavy vehicle is reduced by 40%. Similarly, Bradley [3] also anticipated that a 20% aerodynamic drag reduction on a heavy goods vehicle could lead to 4% of fuel saving during high-speed operation.

Aerodynamics of road vehicles is an active research topic nowadays due to the implementation of stringent regulations in many countries governing noise and exhaust gas emissions. In order to reduce noise and exhaust gas emissions, on top of improving engine technology the aerodynamic efficiency of road vehicles also requires to be improved. Aerodynamic efficiency of small vehicles such as cars and vans have been significantly improved in the last few decades [5]. In addition, the flow pattern over small vehicles has been extensively studied using both simplified models and actual vehicles [5,6]. One of the most common simplified models for investigating the flow physics of small vehicles is the Ahmed body originally proposed and used by Ahmed et al. [7]. Since then, many researchers investigated the flow pattern and drag characteristics over the Ahmed body with various slant angles to study the flow physics of simplified fast-back small vehicles [7–13]. The general time-averaged flow pattern over the wake region of the Ahmed body was concluded by Choi et al. [14]. Basically, the flow pattern is composed of a recirculating bubble on the slant surface and a wake region downstream of the vertical base of the Ahmed body. In addition, a pair of counter-rotating horseshoe vortices emanates from the side edges of the slant surface [14,15]. It was found that minimum drag occurs when the slant angle is 12.5° [14]. At this slant angle, the flow remains attached so that no recirculating bubble is formed on the slant surface of the Ahmed body.

Although the flow characteristics over the Ahmed body have been extensively investigated, the data collected could not be used

* Corresponding author.
E-mail address: kinhing.lo@glasgow.ac.uk (K.H. Lo).

http://dx.doi.org/10.1016/j.expthermflusci.2016.11.003
0894-1777/

to describe the general flow pattern over HGVs. This is because most HGVs have square-back rather than fast-back designs. As a result, another simplified model known as the General Motor (GM) model was used to represent square-back vehicles such as HGVs and buses [16]. The time-averaged flow pattern over the GM model was summarised in [14,16–19]. In general, the location at which flow separation occurs in the GM model is fixed at the sharp rear end. The occurrence of flow separation leads to the formation of a large and three-dimensional recirculating bubble downstream of the vehicle base. In addition, a pair of spanwise, counter-rotating vortices is formed downstream of the base of the GM model. The presence of these vortical structures significantly reduces the base pressure and increases the drag encountered [2,14].

Although the GM model could be used to represent some square-back heavy vehicles, this model could not be used to describe the flow characteristics over articulated lorries or tractor-trailers. Due to this reason, two simplified models known as the Ground Transportation System (GTS) [20–22] and the Generic Conventional Model (GCM) [23,24] were proposed and used to investigate the flow characteristics over articulated lorries. The GTS model represents the Cab-Over-Engine (COE) arrangement of the tractor unit of articulated lorries which is common in Europe. The flow characteristics over an articulated lorry with the COE arrangement is the subject matter of the present study. In contrast, the GCM model represents the conventional tractor unit arrangement which is commonly found in articulated lorries in the United States and Australia. In general, the original GTS model is the most simplified model to investigate the aerodynamic behaviour of articulated lorries. However, the lack of geometric features such as the gap and wheels in the GTS model suggests that the flow pattern over the model is unrealistic. These shortfalls were partially rectified in the modified GTS model [25] through the addition of a gap region and wheels to the model. However, it is still considered as an over-simplified model to be used in studying the aerodynamic characteristics of articulate lorries. In contrast, the GCM and later the modified GCM model [14] are more realistic due to the presence of the gap, wheels and other geometric features in the model.

Nevertheless, previous studies using the GTS and GCM models concluded that four main drag sources could be found in articulated lorries. These four regions are the front stagnation region, the gap flow region, the underbody flow and the large wake region that present downstream of the base of the square-back trailer [26–28]. Various devices and flow control strategies have been proposed in attempt to achieve drag reduction in these areas [14]. Since most of the previous studies mentioned in [14] concerned with the effects of various flow control devices in achieving drag reduction on articulated lorries, the flow physics of these vehicles is less well studied particularly for those articulated lorries with the COE tractor unit arrangement. In general, the time-averaged flow pattern over the modified GCM and GTS models under no crosswind condition could be summarised as follows. The flow stagnates at the front surface and separates at the rear end of the tractor model. Part of the separated flow enters the gap between the tractor base and the front face of the trailer. This results in the formation of a pair of counter-rotating spanwise vortices in the gap region. Along the trailer model, the flow remains attached until it reaches the rear end of the trailer at which massive flow separation appears. As a result, a large three-dimensional wake region is formed downstream of the base of the trailer model [14].

Recently, Mugnaini [29] investigated numerically the flow physics of a generic articulated lorry model with the conventional tractor unit arrangement. However, the results provided in [29] could only be treated qualitatively as the accuracy of the numerical procedures used is unclear. Similarly, Malviya et al. [30] investigated numerically the flow pattern over a generic articulated lorry model with the COE tractor unit arrangement. The result shown in [30] generally agreed with the conclusion drawn by Choi et al. [14]. However, due to the trailer model used in [30] was taller than the tractor model, an additional large recirculation bubble was formed immediately downstream of the front edge on the roof of the trailer model. Again, no information in the numerical scheme accuracy was provided in [30] which means that the data shown could only be understood qualitatively. Buil and Herrer [27] investigated numerically the flow characteristics over a COE typed articulated lorry with a circular-shaped trailer. The general flow pattern over the vehicle remains similar to that shown in an articulated lorry with a box-shaped square-back trailer. Once again, the accuracy of the numerical results shown in [27] is unknown. Altaf et al. [2] investigated numerically the flow pattern over a simplified generic square-back HGV model. Since only velocity and pressure contours were reported; no quantitative data about the characteristics of the wake vortex could be obtained from the study.

The lack of quantitative data in the flow physics of articulated lorries causing two significant problems in studying the aerodynamic properties of articulated lorries. Firstly, as already mentioned that the data presented in [27,29,30] could only be understood qualitatively due to lack of quantitative data available for validating the accuracy of numerical schemes. In addition, the lack of quantitative data also hindered the development of effective flow control devices that could be legally implemented in actual articulated lorries. The primary objective of the present experimental study is to provide some quantitative data in the flow characteristics over the wake region of a 1:20 scale generic articulated lorry model with the COE tractor unit arrangement. The data collected could be used for the purpose of numerical scheme validation and to improve our understanding in the flow physics over actual articulated vehicles with the COE tractor unit arrangement. The flow pattern over the model was visualised using surface oil flow visualisation, smoke visualisation and two-component Particle Image Velocimetry (PIV) techniques.

2. Experimental setup

2.1. Generic articulate lorry model

A 1:20 scale generic articulated lorry model was used in the present experimental study and its schematic is shown in Fig. 1. This model was designed based on some actual articulated lorries that commonly be found in the United Kingdom. Similar scale articulated lorry models also employed by Taubert and Wygnanski [31] and Ortega et al. [32]. It is generally agreed that the flow features appear over the model with this scale are comparable to those shown in the actual articulated lorries [14,31,32]. A normalised gap length ($G/\sqrt{A}$) of 0.1 is maintained between the tractor and the trailer to simulate the vehicle configuration during high-speed operation. It should be noted that G and A are the gap length between the tractor and trailer and the model frontal area, respectively.

2.2. The de Haviland wind tunnel

The present experimental study was conducted using the de Haviland wind tunnel of the University of Glasgow. The wind tunnel has a closed-loop design with a settling chamber to test section contraction ratio of 5:1. The dimensions of the wind tunnel test section are 4.0 m × 2.7 m × 2.1 m (length × width × height). Optical access is achieved through two glass-made side windows and two ceiling mounted Perspex windows. In order to ensure fully turbulent flow was used in the experiments, the freestream velocity

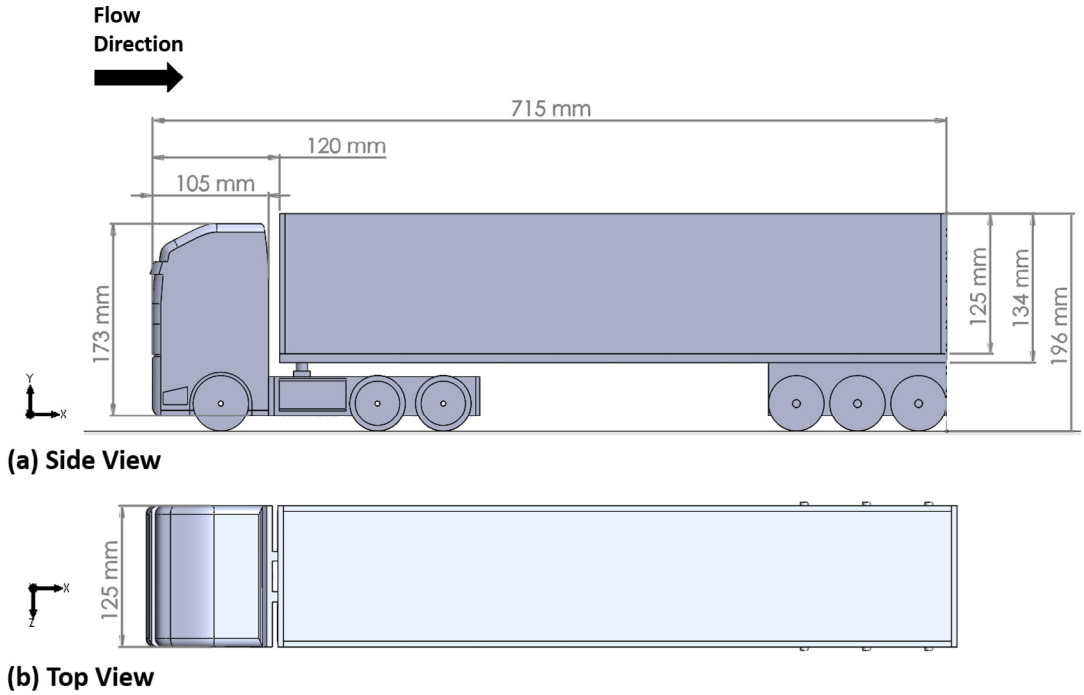

Fig. 1. Schematic of the 1:20 scale articulate model. (a) Side View and (b) Top View.

(U) was set to U = 50 ± 1 ms^{-1}. Through this setting, the flow Reynolds number with respect to the height of the tractor model ($Re_{H\_tractor}$) was $Re_{H\_tractor}$ = 6 x10^5. Although the flow Reynolds number is still an order of magnitude lower than that shown in the actual articulated lorries, Gurlek et al. [15] and Krajnovic and Davidson [33] concluded that the flow features and pressure drag that present over a scale model with $Re_{H\_tractor} > 2.1 \times 10^5$ are comparable to those shown in the actual vehicles. However, it must be emphasised that the skin friction drag acting on an actual articulated lorry is about 5 times higher than that acting on a 1:20 scale model. Since the majority of aerodynamic drag (i.e. about 90%) acting on an articulated lorry comes from the pressure drag; therefore, the effect contributed by the skin friction drag is usually ignored when studying the aerodynamic characteristics of tractor-trailers [14]. It should be noted that the freestream turbulent intensity in the wind tunnel test section at 50 ms^{-1} is about 0.4%.

The articulated lorry model was mounted on a stationary false floor for simulating the boundary conditions encountered by the actual road vehicles. A schematic of the experimental setup is shown in Fig. 2. Similar experimental setups also employed by Gurlek et al. [15], Taubert and Wygnanski [31] and Blocken et al. [34]. The dimensions of the false floor are 1.8 m × 0.8 m × 0.02 m (length × width × thickness). A 200 mm long sharp leading edge is attached at the front of the false floor. It was supported by two pairs of symmetrical aerofoil-shaped supports and was situated at 845 mm above the floor of the test section. The false floor used in this study was designed based on the size of the false floors used in Taubert and Wygnanski [31]. No particular adverse effect caused by the relatively short length of the false floor was reported in [31]. It should be noted that the test section size of the wind tunnel in Taubert and Wygnanski [31] is comparable to the test section size of the de Haviland wind tunnel used in the present study. In addition, Barlow et al. [35] studied the effects of ground clearance in affecting the accuracy of aerodynamic force measurements in road vehicle models in wind tunnel tests. Choi et al. [14] concluded that the ground effect in affecting the aerodynamic characteristics over heavy vehicle models is not as significant as in car and van models due to their high ground clearance (C) to width (W) ratio, C/W. In fact, the C/W ratio is 0.2 in the model used and therefore, the effect of ground clearance is not particularly considered in this study. The articulated lorry model was mounted 450 mm downstream of the false floor leading edge. The blockage ratio of the wind tunnel test section caused by the articulated lorry model and the false-floor was 3.52%.

The boundary layer profile shown in Fig. 3 was measured at the beginning of the tractor model on the false floor. The measured boundary layer profile was compared with the theoretically predicted boundary layer profile using the 1/7th power formula. The boundary layer thicknesses based on 99% of the freestream velocity (δ_{99}), the displacement thickness (δ^*) and the momentum thickness (θ) are δ_{99} = 11.7 mm, δ^* = 0.75 mm and θ = 0.64 mm. This yields a shape factor (H), defined as H = δ^*/θ, of 1.2 which indicates that fully turbulent flow was employed in the present study.

3. Flow diagnostics

3.1. Surface oil flow visualisation

Spanwise flow pattern over the articulated lorry model was examined through surface oil flow visualisation. In-house developed fluorescent oil was used as dye. In order to visualise the flow mixing effect along the articulated lorry model, four colours of fluorescent oil (i.e. white, yellow, orange and pink) were used. The oil was applied to the surface of the model and the false floor by brushes. The locations at which the fluorescent oil was applied is presented in Fig. 4. In order to increase contrast, the false floor and the articulated lorry model were first sprayed with five layers of matt black acyclic paint prior to the experiments. Illumination was provided by a ceiling mounted Ultra-Violet (UV) Light Emitting Diode (LED) flood lamp with peak emission wavelength of 400 nm. The instantaneous oil streaks left on the model and the false floor were captured during wind-on condition using a ceiling

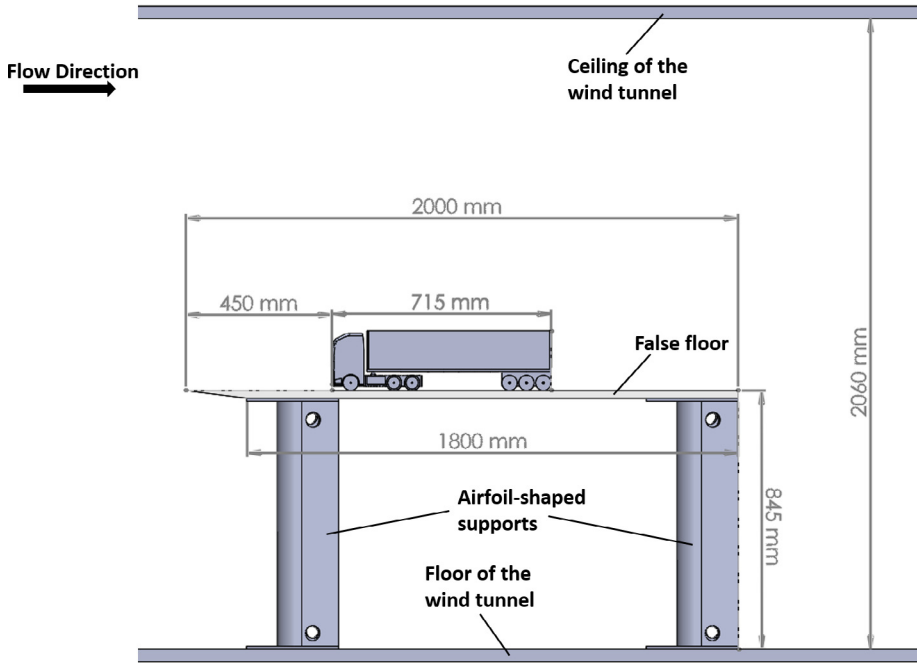

Fig. 2. Schematic of the experimental setup (drawing not to scale).

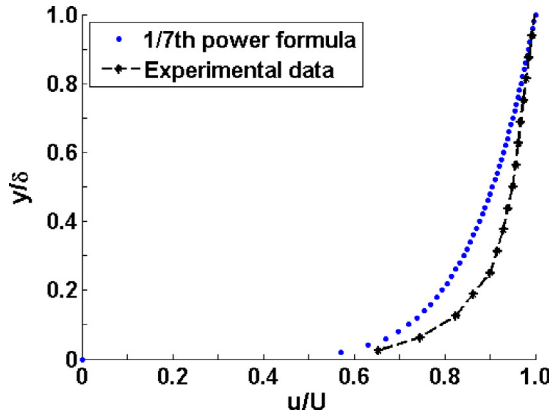

Fig. 3. The measured and predicted boundary layer profiles.

mounted Cannon Single Lense Reflection (SLR), EOS-600D digital camera. The camera has a maximum resolution of 14 megapixels. The ISO speed, shutter speed and the aperture (F) were set to ISO800, 1/400 s and F2.8, respectively. Each set of experiment was repeated three times and approximately 100 wind-on images were captured in each test.

3.2. Smoke visualisation

Smoke visualisation was used to qualitatively visualise the streamwise flow pattern over the articulated lorry model. A Pea Soup SGS-90 smoke machine generated the smoke using the Pea Soup Model 135 Type A smoke oil at a constant flow rate of 80 mL/h. The smoke was delivered to the false floor via a smoke probe. The probe was carefully aligned so that the smoke streaks moved along the centreline of the articulated lorry model. Illumination in the smoke visualisation experiments was achieved using four ceiling mounted 120 W white LED flood lamps. These LED flood lamps uniformly illuminated the entire false floor and the articulated lorry model. Instantaneous smoke streaks over the articulated lorry model were captured using a Photron FastCam SA1.1 high-speed camera with its frame rate and exposure time set to 5000 frame-per-second and 5 μs, respectively.

3.3. Two-component particle image velocimetry measurements

Velocity and vorticity information along the centreline of the articulated lorry model was resolved using the two-component Particle Image Velocimetry (PIV) technique. In addition, the PIV measurements also resolved the x- and y-components of the root-mean-square velocity (u_{rms} and v_{rms}) and Reynolds stress along the xy-plane ($u'v'$) in the flow field. Laser illumination in the PIV measurements was generated by a pair of Litron LPY742-100, Nd:YAG Q-switched lasers with pulse energy and repetition rate of 100 mJ and 200 Hz, respectively. The wavelength of the laser beam is 532 nm and the laser pulse width was 5 ns. The two laser beams were delivered to the ceiling of the wind tunnel through a series of reflective mirrors. A set of lens was used to deflect and expand the laser beams into a thin laser sheet with thickness of approximately 1.5 mm which illuminated along the centreline of the wind tunnel test section.

Olive oil particles with typical diameter of 1 μm was used as the seeder particles. The seeder particles were generated by a PIV Tech aerosol generator with the particle generation rate set to 1×10^8 particles per second. A Phantom v341 high-speed camera was used to capture the scattered light signals reflected from the seeder particles. This camera has a spatial resolution of 2560 pixels × 1600 pixels. A Sigma 105 mm fixed lens with its aperture set to F2.8 was attached to the front of the camera so that a viewing area of 466 mm (length) × 291 mm (height) was provided. A 10 μs time delay between the two laser pulses (Δt) was used in order to ensure sufficient particle movement was achieved between the two frames. It was calculated based on the freestream velocity and the size of the interrogation windows used in the PIV measurements. It should be noted that 2500 image pairs were used to construct the time-averaged vector field in the PIV measurements.

Captured images from the PIV measurements were processed using the cross-correlation algorithm handled by the software

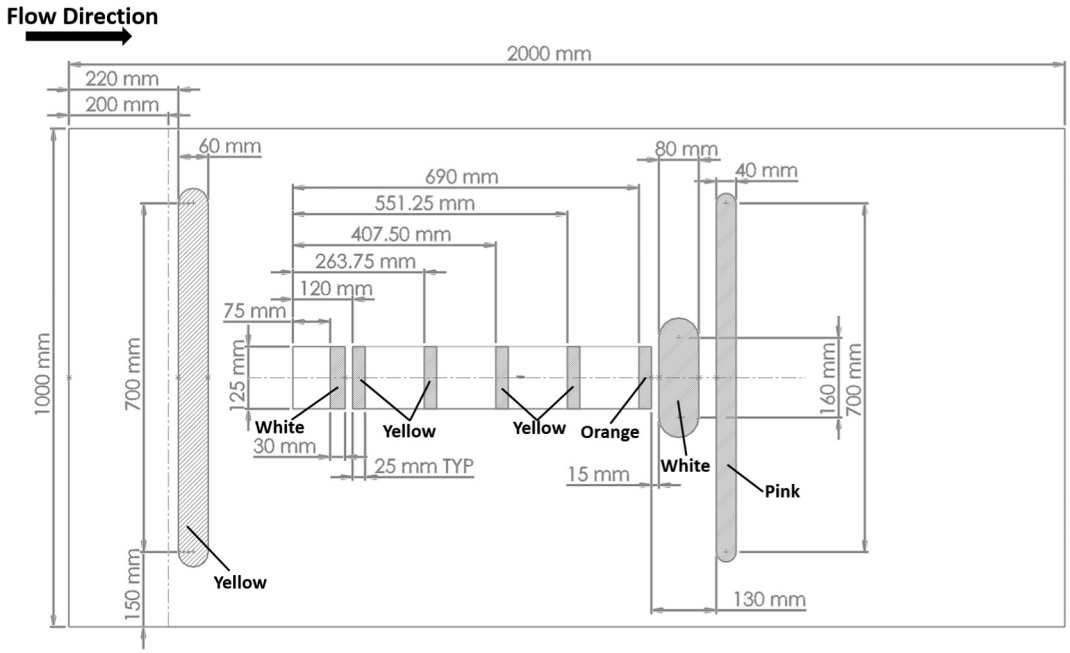

Fig. 4. Locations at which the fluorescent oil with various colours was applied (drawing not to scale).

Davis 8.2. The data of time-averaged velocity components, root-mean-square velocity components, Reynolds stress along the xy-plane and z-vorticity were calculated from the processed PIV data. The algorithms for calculating these parameters could be obtained from [36]. The recorded images were initially divided into a number of 32 pixels × 32 pixels interrogation windows and two passes of cross-correlation were conducted. The interrogation windows were then refined to 16 pixels × 16 pixels and then three additional passes of cross-correlation took place. It should be noted that a 50% overlapping of the interrogation windows was adopted in order to improve spatial resolution and to prevent the appearance of spurious vectors by adaptively improving the interrogation window size [37,38]. Processed PIV data were stored in a Windows-based personal computer and post-processed using the software Tecplot 360.

Uncertainty in the PIV measurements was quantified using the approach developed by Lusk [39] and later adopted by Lo et al. [38] and Lusk et al. [40,41]. The uncertainty of the total number of vectors resolved by the Davis software is about 3% [39]. The Stokes number (Stk) of the seeder particles is $Stk = 1.6 \times 10^{-6}$. Therefore, the uncertainty in the seeder particles to follow the flow streaklines is negligible according to Samimy and Lele [42]. Also, the maximum turbulent level in the flow field is approximately 5%. Since at least 5000 images (i.e. 2500 image pairs) were used to construct the time-averaged vector field and noting that a 95% confident interval was employed; the corresponding uncertainty in the time-averaged PIV measurement due to the presence of turbulent flow in the flow field is about 1.96% calculated using the formula shown in [39]. Therefore, the overall uncertainty (ε) in the PIV measurements is approximately $\varepsilon = \sqrt{0.03^2 + 0.0196^2} = 0.036$ or 3.6%.

4. Results and discussion

4.1. Time-averaged flow field

Qualitative streamwise flow pattern over the articulated lorry model captured from the smoke visualisation experiments is first presented in this subsection. Fig. 5a presents the general streamwise flow pattern over the articulated lorry model. At the front of the tractor model the flow moves upwards and downwards to flow around the tractor model. This upwards and downwards flow movement is separated by a flow streamline with its end known as the stagnation point (ST) as shown in Fig. 5a. Above the stagnation point, the flow expands and accelerates along the curved roof and eventually separates from the rear end of the tractor model. Part of the flow enters the gap region between the tractor and the trailer models while the remaining part of the flow moves along the trailer model. Massive flow separation appears at the rear end of the trailer model (SP) which leads to the formation of the upper shear layer (SL_U) and the wake region downstream of the rear end of the trailer model.

Fig. 5b shows the close-up view of the tractor model and the front part of the trailer model. The presence of the stagnation point (ST) at the front face of the tractor model could be seen clearly. A recirculating bubble (SB) is presented at the beginning of the trailer model which indicates that separated flow appears due to the impingement of the flow with the front sharp edge of the trailer's roof. Fig. 5c displays the recirculating wake region, featured with a large wake vortex (VC), that present downstream of the rear end of the trailer model. The formation of this wake vortex is due to the coil-up of the lower shear layer (SL_L) emanating from the underbody of the trailer model.

The thicknesses and angles of the shear layer as well as the size of the wake vortex were measured using the averaged data collected from 1000 instantaneous smoke visualisation images. The averaged angles, lengths and thicknesses that measured are defined and shown in Fig. 6. The data obtained from the measurements are tabulated in Table 1. From Table 1, it can be seen that the shear layer downstream of the rear end of the trailer model points slightly downwards relatively to the freestream direction. In addition, the wake vortex has an outer diameter (OD) of 94.2 mm which is equivalent to 75.4% of the height of the trailer container model ($H_{container}$) where $H_{container}$ = 125 mm.

Fig. 7 shows the spanwise flow pattern over the articulated lorry model using an image captured from the surface oil flow visualisation experiment. Due to the resource constraint, the

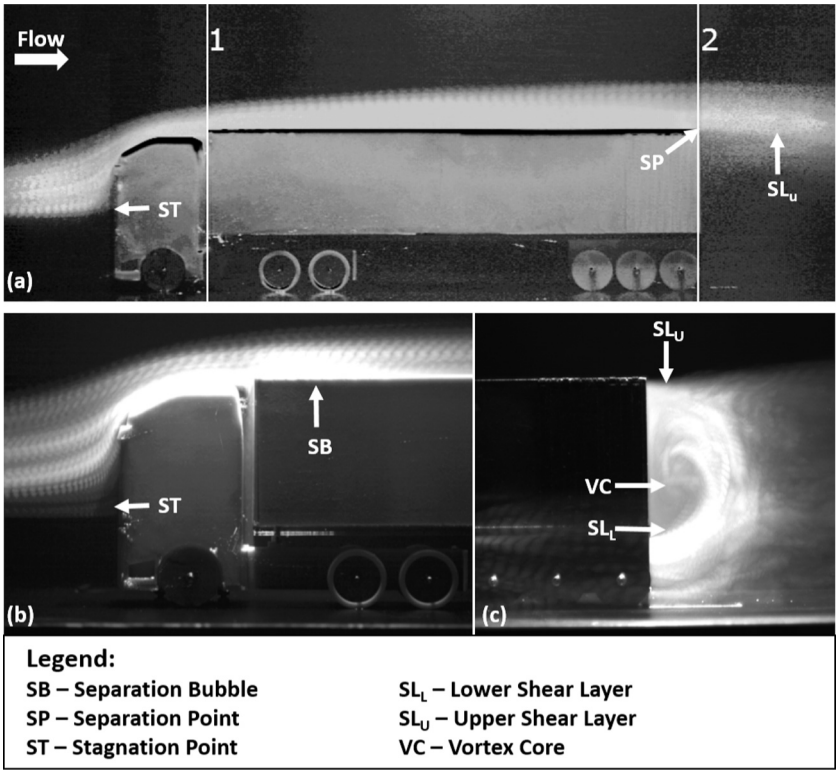

Fig. 5. Streamwise flow pattern over the articulated lorry model. (a) Overall flow pattern and close-up view over the (b) front and (c) rear parts of the model.

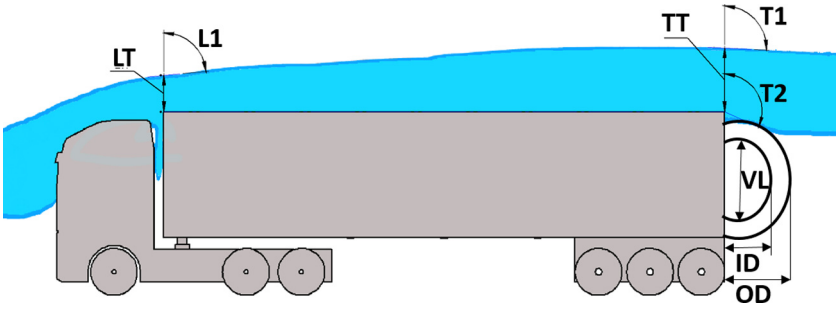

Fig. 6. Definitions of the averaged lengths and angles measured.

Table 1
Averaged angles, thicknesses, lengths and diameters measured at various locations over the articulated lorry model.

LT (mm)	TT (mm)	L1 (degrees)	T1 (degrees)	T2 (degrees)	VL (mm)	ID (mm)	OD (mm)
31.6 ± 2.1	58.6 ± 3.8	84.6 ± 1.0	91.1 ± 0.8	97.9 ± 3.0	51.9 ± 3.5	60.4 ± 2.3	94.2 ± 5.2

illuminating light source was focused to the rear part of the trailer model in the surface oil flow visualisation experiment. As a result, a shadow (SD) appears in front of the tractor model and hence, the stagnation zone location could not be identified in Fig. 7. However, the general spanwise flow pattern over the model could still be observed from Fig. 7. The presence of the stagnation zone at the front of the tractor model forces the incoming flow to move around the tractor model through the two sides. Since the tractor model has a blunt geometry; the flow could not follow the contour downstream of the front of the tractor model. As a result, massive spanwise flow separation appears at the two sides which leads to the formation of two oil-free zones (FS) as shown in Fig. 7.

A pair of counter-rotating spanwise vortices (SV_L and SV_R) is formed immediately downstream of the rear end of the trailer model and similar spanwise vortical structures also documented in [15]. The formation of this spanwise vortex pair is caused by the presence of the low pressure wake region which attracts the flow around to move into and circulate there. The averaged width of the separated flow region and the dimensions of the two spanwise vortices were measured and tabulated in Table 2. The lengths that measured are defined and displayed in Fig. 8. It should be noted that the data shown in Table 2 were obtained from averaging 100 instantaneous images captured from the surface oil flow visualisation experiments. From Table 2, it can be concluded that the flow pattern over the two sides of the articulated lorry model is nearly symmetrical. The averaged length and width of the two spanwise vortices are similar and this finding is agreed with the PIV data shown in [15] using a scale bus model.

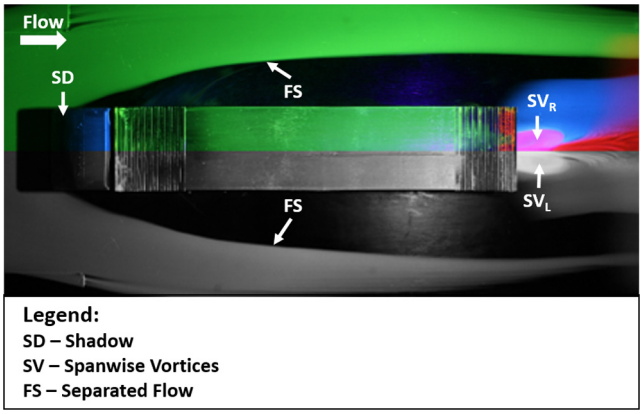

Fig. 7. Spanwise flow pattern over the articulated lorry model.

Fig. 9 presents the time-averaged streamtraces and velocity information over the front and rear parts of the articulated lorry model obtained through two-component PIV measurements.

Normalised coordinates x/H and y/H are used to represent the x- and y-axes in Fig. 9 where H is the height of the trailer container model which is 125 mm. Similarly, the velocity information shown in Fig. 9 is normalised with the freestream velocity (U). Fig. 9a displays the streamtraces and the normalised velocity magnitude contour over the front and the rear end of the articulated lorry model. A small shadow (SD) is shown at the front due to the geometry of the tractor model. However, the presence of this small shadow does not affect the understanding of the flow pattern along the articulated lorry model. From Fig. 9a, it can be seen clearly from the streamtraces that when the incoming flow approaches the front face of the tractor, the flow decelerates so that it could be moved upwards and downwards to avoid the front face of the tractor model. The dividing streamline which separates the upwards and downwards flow regions can be seen in Fig. 9a. The location of the stagnation point (ST) is located at $x/H = -5.6$ and $y/H = 0.05$. Above the stagnation point, the flow accelerates along the roof of the tractor model which is evidenced by the streamtube contraction and the high normalised x-velocity around the tractor roof region shown in Fig. 9a and b, respectively.

Flow separation occurs at the rear of the tractor model and part of the separated flow enters the gap between the tractor and the trailer models which can be seen from the streamtraces shown in Fig. 9a. The flow in the gap region has considerably low normalised x-velocity and highly negative normalised y-velocity as seen in Fig. 9b and c, respectively. The remaining part of the separated flow emanating from the tractor model impinges with the top front edge of the trailer model. A stagnation point (ST_2) is presented at the sharp front edge of the trailer model resulting from this flow impingement as seen in Fig. 9a. A recirculating bubble (SB) is formed in the region between $-4.7 < x/H < -4.3$ and $1 < y/H < 1.05$ immediately downstream of the stagnation point (ST_2) as shown in both Fig. 9a and b. This is agreed with the time-averaged smoke streaks that present along the front part of the trailer model as shown in Fig. 5b.

Massive flow separation appears at the rear end on the roof of the trailer model which can be seen from the streamtraces (Fig. 9a) and the normalised x-velocity contour (Fig. 9b). The occurrence of this flow separation leads to the formation of the upper shear layer downstream of the rear end of the trailer model. In addition, another shear layer, known as the lower shear layer, is presented downstream of the rear end of the trailer's underbody. This lower shear layer is less energetic than the upper shear layer. As a result, the lower shear layer tends to coil-up and forming the counter-clockwise rotating wake vortex downstream of the rear end of the trailer model as shown in Fig. 9a. In fact, similar vortical structure also observed downstream of the rear end of a scale bus model documented in [15]. Returning to the wake vortex, from Fig. 9a, it can be seen that its vortex core (VC) is located at the normalised location $x/H = 0.2$ and $y/H = 0.25$. It was measured that the length of the wake vortex is about 70% of the height of the trailer container model which is comparable to the data presented in Table 1.

Flow characteristics within the wake vortex can be further quantified by considering the velocity profiles along the wake region downstream of the trailer model. Fig. 10 presents the time-averaged normalised x- and y-velocity profiles measured at various normalised transverse locations (x/H) along the wake region. Fig. 10a–d show the normalised x-velocity profile (u/U) measured at the normalised x-locations, $x/H = 0.2$, 0.5, 0.8 and 1.1 along the wake region. At $x/H = 0.2$ (Fig. 10a), positive normalised x-velocity is shown in the region between $-0.5 < y/H < 0.2$ due to the jet-like flow emerges from the rear end of the trailer's underbody. The highest positive normalised x-velocity appears at the normalised y-location $y/H = -0.2$ with its magnitude $u/U = 0.28$. Negative normalised x-velocity is shown in the region between $0.2 < y/H < 0.85$ which indicates that reverse flow is presented in the wake region. In fact, minimum normalised x-velocity appears at the normalised y-location $y/H = 0.5$ with its magnitude $u/U = -0.1$. Fig. 10b presents the normalised x-velocity profile measured at $x/H = 0.5$. At this location, the positive normalised x-velocity between $-0.5 < y/H < 0.2$ becomes weaker compared to that shown in $x/H = 0.2$. Reverse flow still occurs in the region between $0.2 < y/H < 0.85$ within the wake vortex. However, at the normalised x-location $x/H = 0.5$, minimum normalised x-velocity is shown in both $y/H = 0.5$ and 0.8 with its magnitude $u/U = -0.12$. This suggests that stronger reverse flow is presented within the wake region at $x/H = 0.5$ than that shown when $x/H = 0.2$.

Fig. 10c displays the normalised x-velocity profile measured at $x/H = 0.8$. At this location, the positive normalised x-velocity that previously occurred between $0.2 < y/H < 0.85$ disappears. This is because the jet-like flow from the trailer's underbody exerts no effect at this location as it is far away from the rear end of the trailer model. In contrast, reverse flow exists in the entire wake region between $-0.5 < y/H < 0.85$. The lowest normalised x-velocity is presented at the normalised y-location $y/H = 0.7$ with its magnitude remains at approximately $u/U = -0.12$. Fig. 10d shows the normalised x-velocity profile measured at $x/H = 1.1$. The x-velocity profile measured at this normalised x-location remains similar to that shown when $x/H = 0.8$. At $x/H = 0.8$ (Fig. 10c), it can be seen that zero or negative normalised x-velocity presents in the region between $-0.5 < y/H < 0.85$. Interestingly, at $x/H = 1.1$ (Fig. 10d), minimum normalised x-velocity appears at the normalised y-location $y/H = -0.5$ with its magnitude $u/U = -0.1$. The considerably strong reverse flow appears near the ground at

Table 2
Averaged width of the separated flow region and the size of the two spanwise vortices measured at the rear end of the trailer model.

LBL (mm)	RBL (mm)	LVL (mm)	RVL (mm)	LVW (mm)	RVW (mm)
100.6 ± 2.8	95.7 ± 4.3	74.0 ± 3.0	72.8 ± 3.6	33.2 ± 1.8	32.9 ± 2.4

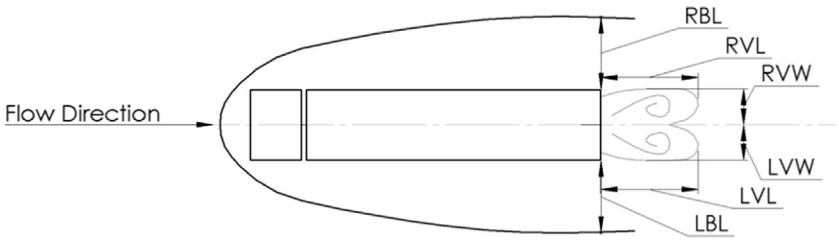

Fig. 8. Definitions of the lengths and widths that measured from averaging a hundred instantaneous images captured from the surface oil flow visualisation experiments.

x/H = 1.1 is caused by the presence of the low pressure wake region which attracts the flow downstream to move into it.

Fig. 10e–h display the normalised y-velocity (v/U) measured at various normalised x-locations along the wake region. In general, negative normalised y-velocity, i.e. downwards flow movement, occurs in the region between 0.9 < y/H < 1.5 in all four normalised x-locations being studied. This indicates that the upper shear layer that formed as a result of the flow separation points downwards which is agreed with the data presented in Table 1. In fact, from Fig. 10e to h, the variation of the normalised y-velocity within the wake region, i.e. the region between 0.2 < x/H < 1.1 and −0.5 < y/H < 0.85, can be generalised as follows. The maximum positive normalised y-velocity increases significantly from v/U = 0.075 at x/H = 0.2 and y/H = −0.15 (Fig. 10e) to reach the peak at x/H = 0.5 and y/H = 0.15 with its magnitude v/H = 0.24 (Fig. 10f). Downstream of x/H = 0.5, the normalised y-velocity reduces progressively. In fact, at x/H = 0.8 and 1.1, the maximum normalised y-velocity at these two normalised x-locations are v/U = 0.12 and 0.09, respectively.

4.2. Instantaneous flow field

After considering the time-averaged flow field, some additional data regarding the instantaneous streamwise flow pattern over the rear end of the trailer model are presented. Fig. 11 shows the development and evolution of the upper and lower shear layers and the wake vortex through a series of instantaneous images captured from the smoke visualisation experiments. The images shown in Fig. 11 concluded that the instantaneous flow pattern over the rear end of the trailer model is considerably different from that shown in the time-averaged flow field. This is expected due to the unsteady nature of the flow over three-dimensional bluff bodies. Fig. 11a shows the flow pattern when the reference time (t) is at t = 0 ms. Flow features appear at this time step are characterised by the presence of a relatively stable upper shear layer (SL_U) and a fully developed wake vortex (SV_L), formed by the coil-up of the lower shear layer (SL_L). The wake vortex is approaching the upper shear layer but no physical contact between these two flow features is observed. At t = 2 ms (Fig. 11b), the wake vortex (SV_L) contacts and interacts with the upper shear layer (SV_U). As a result, the upper shear layer begins to show some flapping motion that leads to the formation of a streamwise vortex (SV_u) in the upper shear layer. This newly formed streamwise vortex grows and propagates downstream along the upper shear layer which can be seen clearly when the reference time is at t = 4 ms (Fig. 11c). At this time step, the flapping motion of the upper shear layer continues while the wake vortex SV_L starts to distort after interacting with the upper shear layer.

At t = 6 ms (Fig. 11d), the first streamwise vortex (SV_u) in the shear layer continues to propagate downstream. The continuous flapping of the upper shear layer leads to the formation of the second streamwise vortex in the shear layer. However, the wake vortex (SV_L) becomes more distorted and starts to become diffuse. At t = 8 ms (Fig. 11e), the two streamwise vortices in the upper shear layer (SV_u) remain clearly defined and their sizes reached the maximum. However, the wake vortex (SV_L) becomes highly distorted and diffuse. At t = 10 ms (Fig. 11f), the highly diffuse wake vortex (SV_L) has already dissipated most of its energy to the upper shear layer. As a result, the flapping motion of the upper shear layer starts to reduce which is evidenced by the size reduction of the two streamwise vortices (SV_u) that present in the upper shear layer.

When the reference time reached t = 12 ms (Fig. 11g), basically the wake vortex (SV_L) can only be seen barely as most of its energy has been dissipated. The upper shear layer is still flapping slowly and the size of the two streamwise vortices (SV_u) remains similar to those shown at t = 10 ms (Fig. 11f). Fig. 11h and i show the streamwise flow pattern at t = 14 and 15.2 ms, respectively. In general, these two time steps mark the end of a cycle of the wake vortex and the upper shear layer interactions, the wake vortex is visually disappeared. The shear layer returns to relatively steady again with its flapping motion ceased. In contrast, the lower shear layer (SL_L) starts to emerge from the trailer underbody. This newly emerged lower shear layer begins to coil-up to form another wake vortex and the next cycle of the wake vortex and the upper shear layer interactions begins.

Fig. 12 presents the instantaneous streamtraces, normalised velocity magnitude and z-vorticity contours at and downstream of the rear end of the trailer model measured using PIV.

Fig. 12a presents the streamtraces, the normalised velocity magnitude and the z-vorticity contours captured at the frame number N = 1. Instead of only one large wake vortex is formed in the wake region as shown in the time-averaged flow field (Fig. 9a), two streamwise vortices (V1 and V2) are presented downstream of the trailer model in the instantaneous streamtraces and the normalised velocity magnitude contour (|U|/U). In fact similar instantaneous streamwise flow pattern also documented in [15] using a scale bus model. In addition, the vortex shedding phenomenon of the upper shear layer was clearly captured in the instantaneous z-vorticity contour (ω) shown in Fig. 12a. The vortex shedding pattern shown in Fig. 12a is comparable to that shown in Fig. 11 when the instantaneous smoke streaks downstream of the rear end of the trailer model were considered. Fig. 12b shows the instantaneous streamwise flow pattern captured at N = 6. The instantaneous streamtraces still show two vortices (V1 and V2) in the wake region although the upper vortex (V2) moves to a further downstream location compared to that shown when N = 1 (Fig. 12a). In addition, the strength of the upper second vortex (V2) seems to be relatively weak as it could not be resolved in the normalised velocity magnitude contour. Moreover, the vortex shedding pattern of the shear layer in the z-vorticity contour shown in Fig. 11a when N = 1 becomes less clearly defined in the present frame. This is deduced that the present frame captured the end of the cycle of the wake vortices and the upper shear layer interactions which previously discussed in Fig. 11h and i.

Fig. 12c and d present the instantaneous streamwise flow pattern captured at the frame numbers N = 15 and 16, respectively.

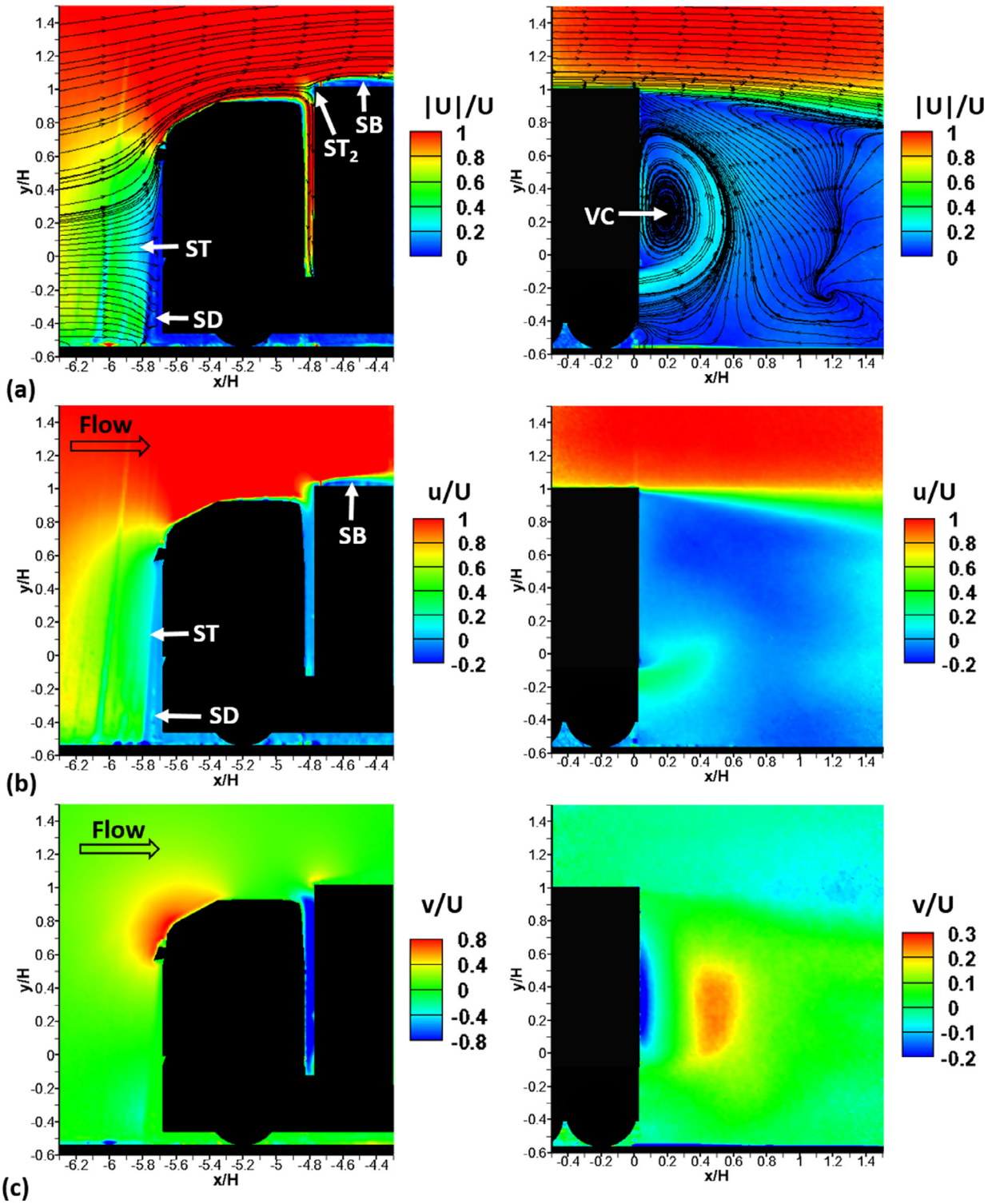

Fig. 9. Velocity contours over the front and rear parts of the articulated lorry model. (a) normalised velocity magnitude with streamtraces, (b) normalised velocity in x-direction and (c) normalised velocity in y-direction.

From the instantaneous streamtraces shown in these two frames, it is clear that the second upper vortex V2 is situated immediately above and downstream of the primary wake vortex V1. The size of the second upper vortex V2 increases when the frame number is progressed from N = 15 to N = 16. In addition, the second streamwise vortex (V2) moves slightly downstream in the frame N = 16 from its location shown in N = 15. This can be clearly seen when comparing both the streamtraces and the normalised velocity magnitude contours between N = 15 and 16 as shown in Fig. 12c and d, respectively. From the instantaneous z-vorticity contours shown in Fig. 12c and d, it can be seen that the vortex shedding pattern of the upper shear layer re-appears in the present two frames. The two streamwise vortices within the upper shear layer in the frame N = 16 (Fig. 12d) are located slightly down-

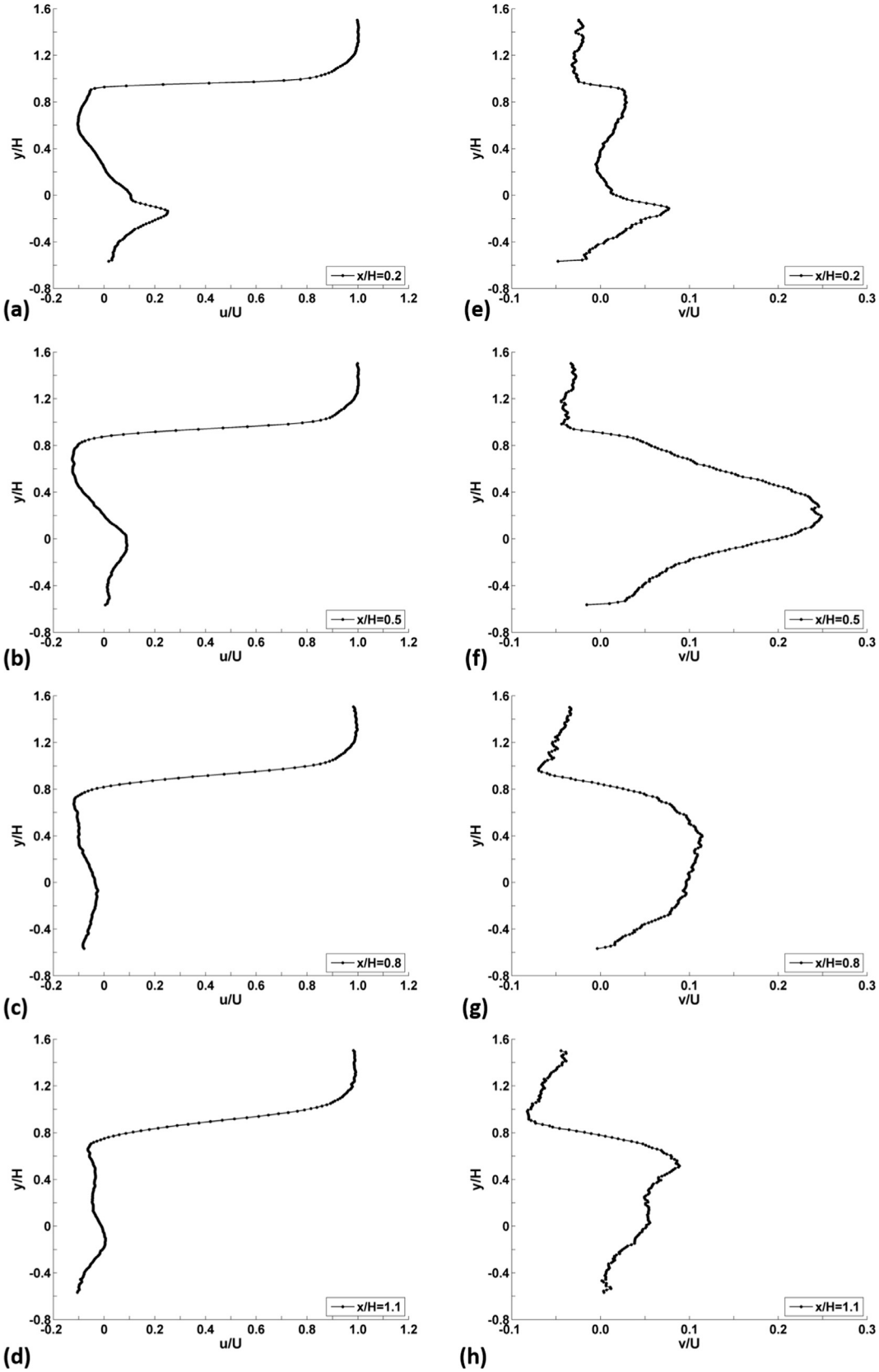

Fig. 10. Normalised x- and y-velocity profiles. (a to d) Normalised x- and (e to h) y-velocity profiles measured at x/H = 0.2, 0.5, 0.8 and 1.1, respectively.

stream of those shown when N = 15 (Fig. 12c). It is believed that the PIV data shown in these two frames present the beginning of the interactions between the wake vortex and the upper shear layer. Further investigation using high-speed PIV in various planes is recommended in order to fully resolve the instantaneous flow pattern over the rear end of the trailer model.

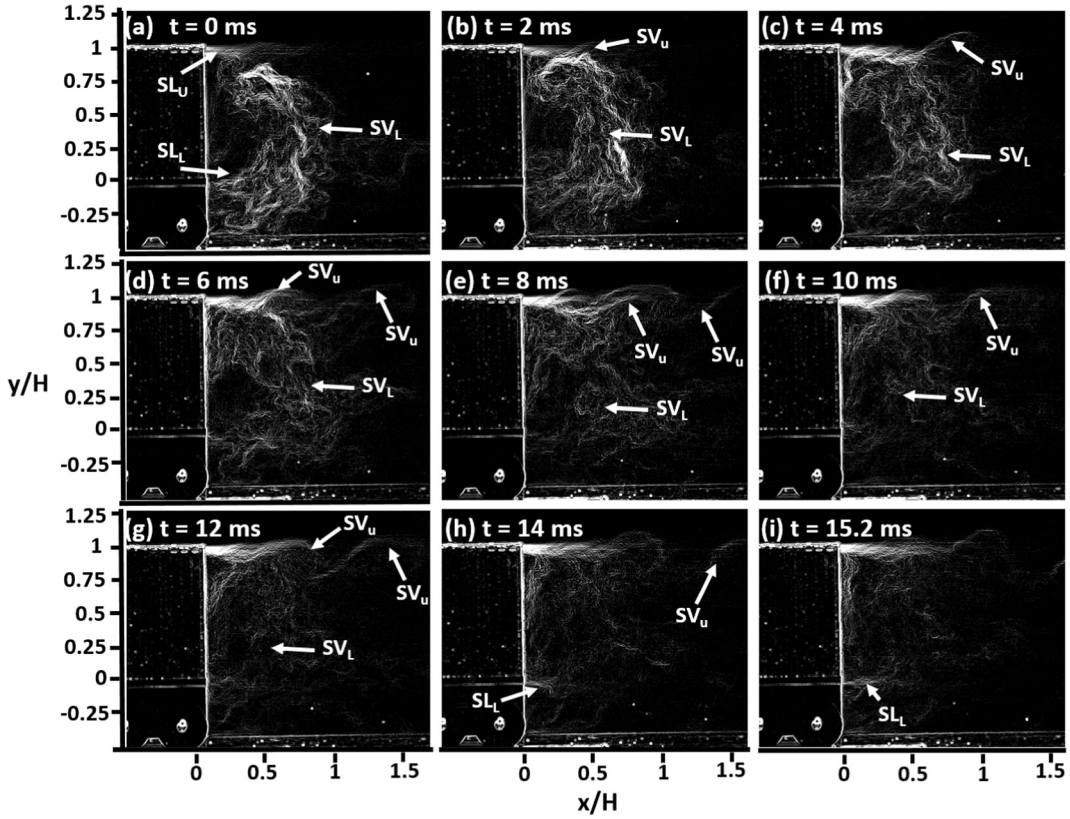

Fig. 11. Instantaneous streamwise flow pattern over the rear of the trailer model. Image captured at the time: (a) 0 ms, (b) 2 ms, (c) 4 ms, (d) 6 ms, (e) 8 ms, (f) 10 ms, (g) 12 ms, (h) 14 ms and (i) 15.2 ms. It should be noted that H = 125 mm.

4.3. Flow turbulent level and vorticity information

Flow turbulent level and vorticity information along the wake region of the trailer model is presented in this subsection. The contours of the normalised rms x- and y-velocity (u_{rms}/U and v_{rms}/U), normalised Reynolds stress along the xy-plane ($u'v'/U^2$) and the z-vorticity (ω) measured at and downstream of the rear end of the trailer model are presented in Fig. 13a–d, respectively.

From Fig. 13a and b, it can be seen that high levels of normalised rms velocity in both x- and y-directions appear along the shear layer downstream of the trailer model. This indicates that the flow within the shear layer is highly turbulent. Moderate levels of normalised rms velocity in both x- and y-directions are presented in the wake region between $0 < x/H < 0.2$ and $-0.1 < y/H < 1$. This suggests that moderately turbulent flow is presented within the wake region. Fig. 13c shows that negative normalised Reynolds stress is presented along the shear layer. This further suggests that the flow within the shear layer is highly turbulent. In contrast, moderate levels of positive Reynolds stress exist in region between $0 < x/H < 1.3$ and $-0.2 < y/H < 0.7$ which means that the flow within and immediately downstream of the wake region is moderately turbulent. From the z-vorticity contour (Fig. 13d), it can be seen that negative z-vorticity is shown along the upper shear layer. In contrast, negative z-vorticity is presented along the lower shear layer downstream of the trailer underbody and the formation of the wake vortex due to the coil-up of the lower shear layer can be clearly seen.

The turbulent characteristics of the flow within the wake vortex can be further quantified by plotting the normalised rms velocity, Reynolds stress along the xy-plane and z-vorticity profiles along the wake region. Fig. 14 shows the normalised rms x- and y-velocity (u_{rms}/U and v_{rms}/U) profiles measured at various normalised x-locations along the wake region. The corresponding profiles of the normalised Reynolds stress along the xy-plane ($u'v'/U^2$) and the z-vorticity (ω) are presented in Fig. 15. From Fig. 14, it can be seen that for all normalised x-locations being studied, high levels of rms velocity in both x- and y-directions appear along the upper shear layer (i.e. the region between $-0.9 < y/H < 1$ at $x/H = 0.2$ and grows progressively to $-0.6 < y/H < 1$ at $x/H = 1.1$). The levels of the rms velocity in both x- and y-directions within the upper shear layer increases progressively from the normalised x-location $x/H = 0.2$ (Fig. 14a and e) to reach their peaks at $x/H = 1.1$ (Fig. 14d and h). This indicates that the flow within the upper shear layer becomes progressively more turbulent. Similar effects could also be observed when considering the normalised Reynolds stress profiles shown in Fig. 15a–d. It can be seen that the levels of the negative Reynolds stress within the upper shear layer increases progressively when the measurement is taken further downstream of the rear end of the trailer. In fact, maximum normalised rms velocity in both x- and y-directions as well as the minimum normalised Reynolds stress are all occurred at the normalised locations $x/H = 1.1$ and $y/H = 0.9$ with their corresponding magnitudes equal to $u_{rms}/U = 0.22$, $v_{rms}/U = 0.19$ and $u'v'/U^2 = -0.018$.

In contrast, weaker velocity fluctuation and turbulent levels are observed within the wake region (i.e. the region between $-0.5 < y/H < 0.85$). The levels of normalised rms velocity in x-direction within the wake region remain between $0.06 < u_{rms}/U < 0.14$ in all normalised x-locations being studied (Fig. 14a–d). Similar trend also shown in the normalised rms y-velocity profiles (Fig. 14e–h) with the levels of v_{rms}/U remain in the range between $-0.06 < v_{rms}/U < 0.13$. In addition, considerably low levels of normalised Reynolds stress along the xy-plane appear in the wake region (Fig. 15a to d). The peak normalised

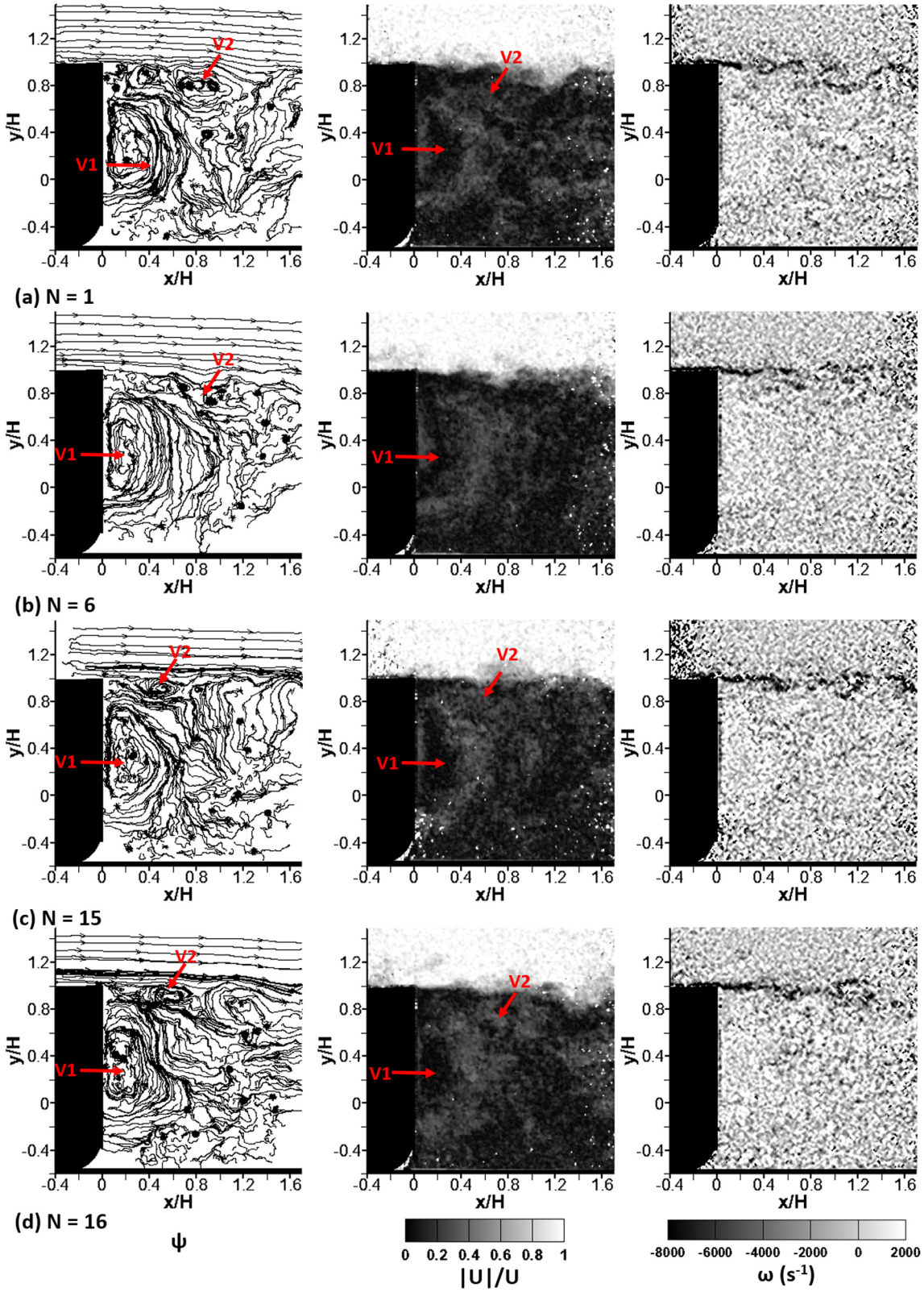

Fig. 12. Instantaneous streamtraces, velocity magnitude and z-vorticity information obtained from PIV measurements. Image captured at the frame number N = (a) 0, (b) 6, (c) 15 and (d) 16.

Reynolds stress along the xy-plane appears at the location of x/H = 0.5 and y/H = 0.4 with its magnitude $u'v'/U^2 = 0.003$ which indicates that moderately turbulent flow appears within the wake region downstream of the trailer model.

Fig. 15e–h show the z-vorticity profiles (ω) along the wake region. In general, high levels of negative z-vorticity appear along the upper shear layer. However, the levels of negative z-vorticity along the upper shear layer decrease progressively when the

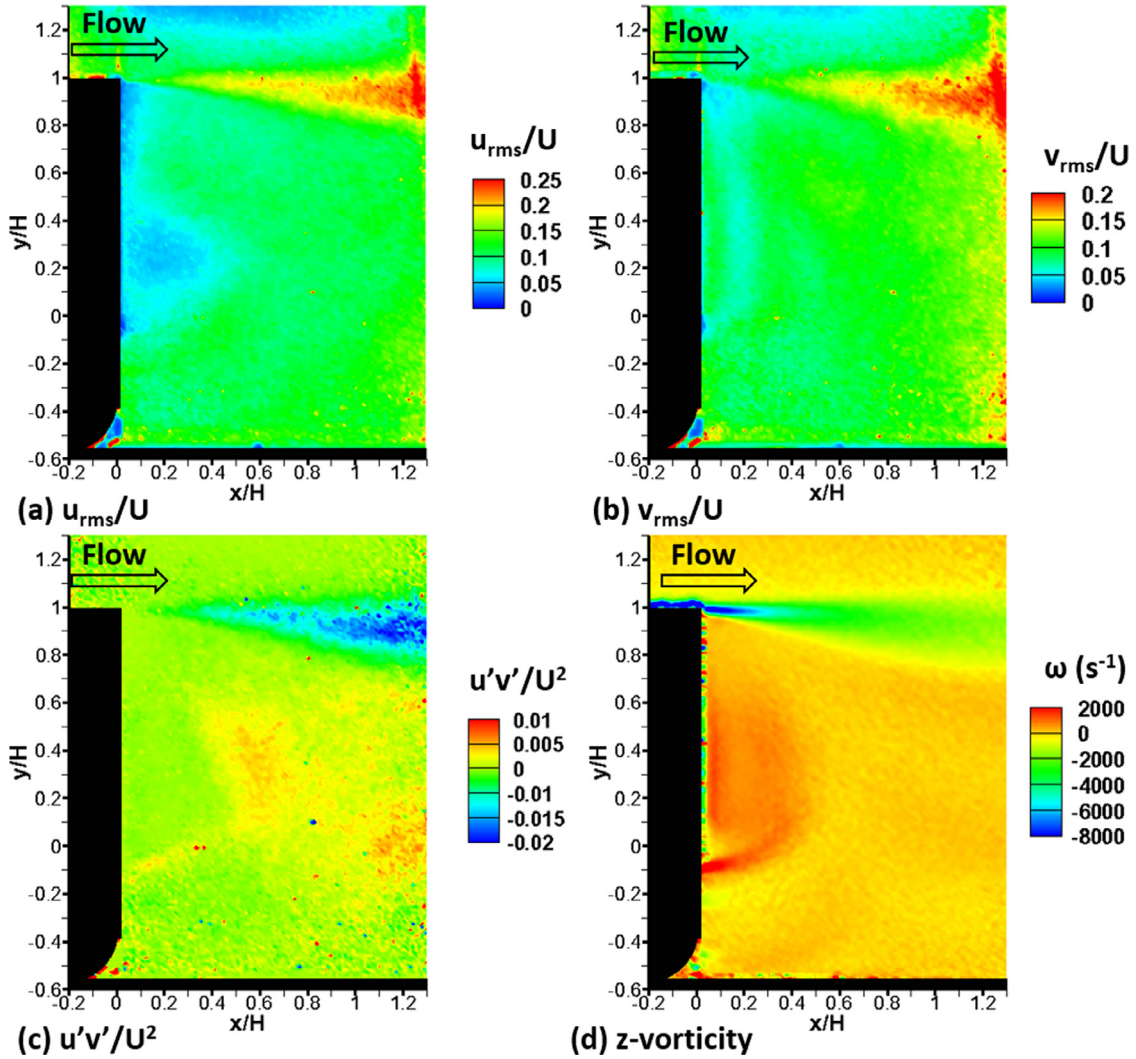

Fig. 13. Contour plots over the rear end of the articulated vehicle model. (a) Normalised root-mean-square velocity in x-direction, (b) normalised root-mean-square velocity in y-direction, (c) normalised Reynolds stress in the xy-plane and (d) z-vorticity.

normalised transverse distance from the rear end of the trailer model increases. In contrast, the width of the region that shows strong negative z-vorticity increases with increasing distance from the rear end of the trailer.

In fact, the highest negative z-vorticity appears at the normalised x- and y-locations x/H = 0.2 and y/H = 0.85 (i.e. in the upper shear layer) with its magnitude $\omega = -7000\ s^{-1}$. Nevertheless, the data shown concluded that the flow within the upper shear layer is highly rotational. Below the shear layer, the levels of z-vorticity in the wake region remain considerably low with an exception when the normalised x-location is at x/H = 0.2 (Fig. 15e). A region that shows moderate levels of positive z-vorticity is presented between $-0.2 < y/H < 0.6$ with its peak magnitude approximately equal to $\omega = 1000\ s^{-1}$. This is due to the presence of the lower shear layer and the wake vortex which gives moderate levels of positive z-vorticity at that region.

4.4. Limitation of the study and future research recommendations

Although the time-averaged and instantaneous flow pattern over the 1:20 scale tractor-trailer model has been investigated, there are three major limitations exist in the present study. Firstly, the sting balance available in the wind tunnel used could not provide sufficient resolution to resolve the drag force acting on the scale tractor-trailer model due to its relatively small size. Therefore, drag data could not be provided in the present study. Secondly, due to the size limitation of the windows and lack of mounting points available in the wind tunnel test section, the flow characteristics further downstream of the trailer model (i.e. anywhere more than 250 mm downstream of the trailer model) and the false floor could not be visualised and measured in the present study. This means that any flow interactions between the lower and the upper parts of the flow downstream of the rear end of the false floor could not be resolved and investigated. Thirdly, due to the design constraint of the existing rail system for holding the laser head used in the PIV measurements, currently only PIV in the streamwise direction along the centreline of the tractor-trailer model could be investigated.

As a result of these three shortfalls, the authors would like to recommend that further investigation, in both time-averaged and instantaneous senses, in the following areas should be conducted: (i) drag measurement, (ii) PIV measurements in other planes and (iii) to investigate the flow physics further downstream of the trailer model. The authors would be highly appreciated if other researchers currently working on similar studies could provide some additional data using the articulated lorry model employed in this study so that the flow characteristics over the entire tractor-trailer model could be resolved.

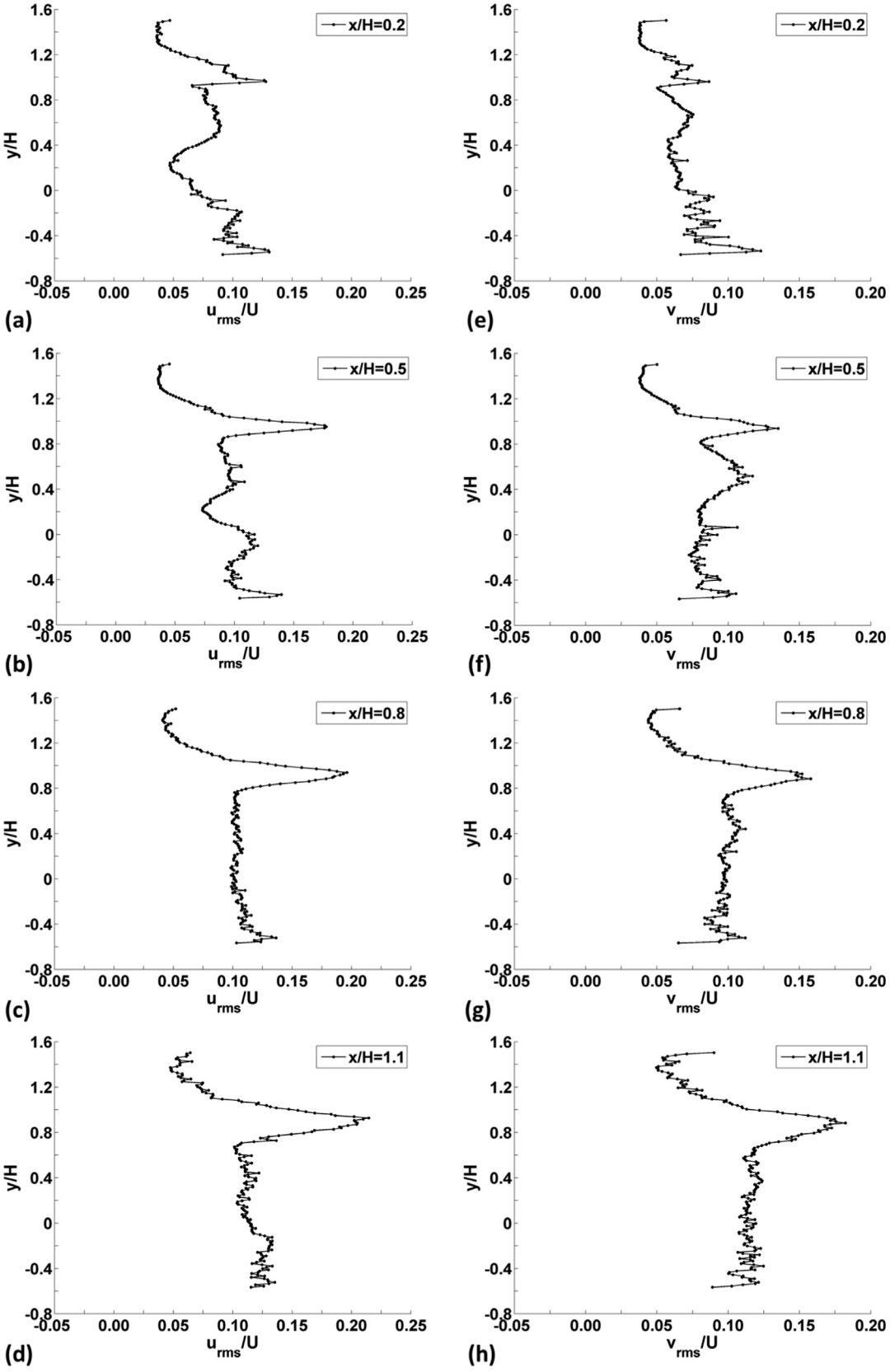

Fig. 14. Normalised root-mean-square x- and y-velocity profiles. (a–d) Normalised rms x- and (e–h) normalised rms y-velocity profiles measured at x/H = 0.2, 0.5, 0.8 and 1.1, respectively.

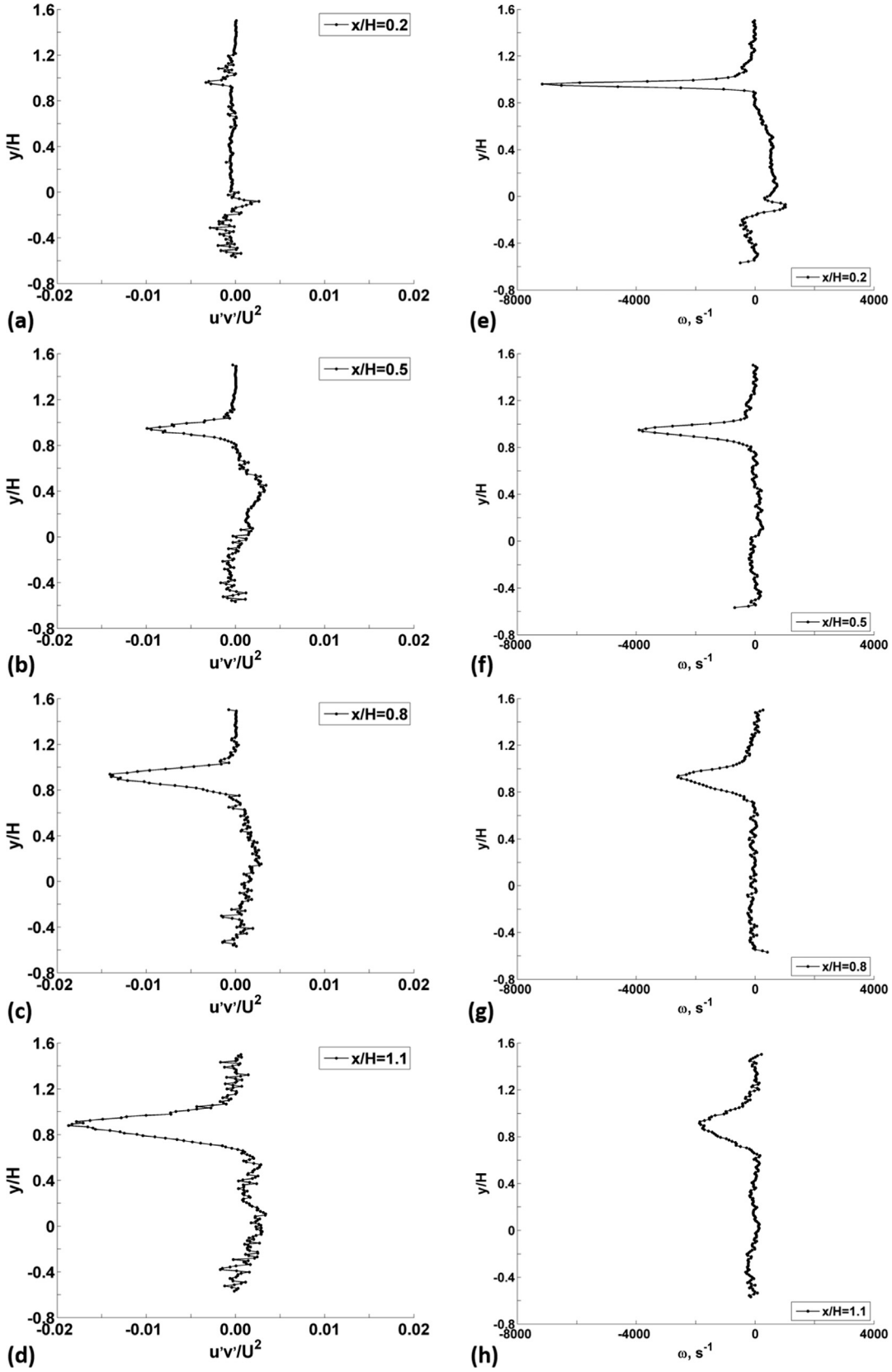

Fig. 15. Normalised Reynolds stress in the xy-plane and z-vorticity. (a–d) Normalised Reynolds stress and (e–h) z-vorticity profiles measured at x/H = 0.2, 0.5, 0.8 and 1.1, respectively.

5. Conclusions

An experimental study has been conducted to investigate both the time-averaged and instantaneous flow pattern over a 1:20 scale articulated lorry model. The de Haviland wind tunnel was used to generate the 50 ms^{-1} freestream adopted in this study. The corresponding flow Reynolds number with respect to the height of the tractor model was 6×10^5. Smoke visualisation, surface oil flow visualisation and particle image velocimetry measurement were employed for flow diagnostics.

The result obtained from the smoke visualisation experiment concluded that a stagnation zone appeared at the front face of the tractor model. In addition, a small separation bubble was found at the beginning of the trailer model resulting from the flow impingement with the sharp front edge of the trailer roof. Massive flow separation was observed at the rear end of the trailer model. As a result, a slightly downwards pointing shear layer and a large counter-clockwise rotating wake vortex were formed downstream of the rear end of the trailer model. It was measured that the length of the wake vortex was about 75% of the height of the trailer container model.

The time-averaged results obtained from the surface oil flow visualisation experiments show that the flow pattern along the two sides of the articulated lorry model was nearly symmetrical. It was found that massive spanwise flow separation appeared at the beginning of the tractor model and therefore, two oil-free regions were shown at the two sides along the model. At the rear end of the trailer model, a large pair of counter-rotating spanwise vortices was observed. The formation of this pair of vortices is caused by the presence of the low pressure wake region downstream of the rear end of the trailer model which attracts the flow around to circulate within it.

The time-averaged data obtained from the two-component particle image velocimetry measurements concluded that a stagnation point is presented at the front of the tractor model and its location was found to be approximately at $x/H = -5.6$ and $y/H = -0.05$. A second stagnation point was observed at the sharp front edge of the trailer roof due to the flow impingement. It was confirmed from the normalised velocity magnitude and x-velocity contours that a separation bubble was formed at the front portion of the trailer model. At the rear end of the trailer model, the presence of the massive flow separation there caused the formation of a large counter-clockwise rotating wake vortex downstream of the rear end of the trailer model. The vortex core of this wake vortex was located at the normalised x- and y-locations of $x/H = 0.2$ and $y/H = 0.25$. The formation of this wake vortex is caused by the coil-up of the relatively low energy lower shear layer emanated from the underbody of the trailer model. The normalised x-velocity profiles obtained along the wake region indicated that considerably strong reverse flow occurred in the wake vortex. In addition, highly turbulent and rotational flow was observed along the upper shear layer. In contrast, moderate levels of rms velocity, Reynolds stress and z-vorticity were shown in the wake region which indicated that the flow was moderately turbulent and rotational. The lower shear layer that emanated from the underbody of the trailer model showed moderate levels of positive z-vorticty.

The instantaneous streamwise flow pattern over the rear end of the trailer model was considerably different from that shown in the time-averaged flow field. The instantaneous smoke visualisation images showed that the interactions between the wake vortex and the upper shear layer led to the formation of a series of streamwise vortices in the shear layer. It was observed that these streamwise vortices grew progressively when they propagated downstream along the upper shear layer. It was found that the energy within the wake vortex seems to be transferred to the upper shear layer to facilitate the streamwise vortices formation. The cycle of the wake vortex and the upper shear layer interactions ended when all the energy in the wake vortex is consumed. Finally, the instantaneous streamwise flow pattern resolved through two-component particle image velocimetry measurements showed that two streamwise vortices were formed in the wake region. The upper second vortex was smaller than the lower primary vortex although its size increased with time. In addition, the vortex shedding phenomenon along the upper shear layer was clearly captured in the instantaneous z-vorticity contour. It is recommended that drag measurements and particle image velocimetry measurements in various planes and locations downstream of the articulated lorry model should be conducted in order to fully resolve the flow characteristics along the wake region.

Author contributions

Experiments and data analysis were conducted by Kin Hing Lo. Manuscript preparation and editing work were jointly done by Kin Hing Lo and Konstantinos Kontis.

Conflicts of interest

The authors declare no conflict of interest.

Acknowledgments

The authors would like to acknowledge the assistance provided by Alphonsus Li Wei Sim and Angel Zarev in the present study. The authors also would like to acknowledge the Engineering and Physical Sciences Research Council – United Kingdom for sponsoring the National Wind Tunnel Facility used in this research project (EPSRC award no.: EP/L024888/1).

References

[1] Transport Statistics Great Britain 2015, Department of Transport, United Kingdom Government, United Kingdom, 2015.
[2] A. Altaf, A.A. Omar, W. Asrar, Passive drag reduction of square back road vehicles, J. Wind Eng. Ind. Aerodyn. 134 (2014) 30–43.
[3] R. Bradley, Technology Roadmap for the 21st Century Truck Program Tech. Rep. 21 CT-001, United States Department of Energy, Washington DC, United States, 2000.
[4] F.-H. Hsu, R.L. Davis, Drag reduction of tractor-trailers using optimized add-on devices, J. Fluid Eng. 132 (2010) 0845041–0845046.
[5] W.-H. Hucho, G. Sovran, Aerodynamics of road vehicles, Annu. Rev. Fluid Mech. 25 (1993) 485–537.
[6] W.-H. Hucho, Commercial vehicles, in: Aerodynamics of Road Vehicles, fourth ed., SAE International, Warrendale, Pa., United States, 1998, pp. 131–237.
[7] S.R. Ahmed, G. Ramm, G. Faltin, Some Salient Features of the Time Averaged Ground Vehicle Wake, SAE Paper, 1984. 840300.
[8] G. Vino, S. Watkins, P. Mousley, J. Watmuff, S. Prasad, Flow structures in the near-wake of the Ahmed model, J. Fluids Struct. 20 (2005) 673–695.
[9] T. Tunay, B. Sahin, V. Ozbolat, Effects of rear slant angles on the flow characteristics of Ahmed body, Exp. Therm. Fluid Sci. 57 (2014) 165–176.
[10] W. Meile, T. Ladinek, G. Brenn, A. Rappenhagen, A. Fuchs, Non-symmetric bi-stable flow around the Ahmed body, Int. J. Heat Fluid Flow 57 (2016) 34–47.
[11] J. Keogh, T. Barber, S. Diasinos, G. Doig, The aerodynamic effects on a cornering Ahmed body, J. Wind Eng. Ind. Aerodyn. 154 (2016) 34–46.
[12] E. Fares, Unsteady flow simulation of the Ahmed reference body using a lattice Boltzmann approach, Comput. Fluids 35 (2006) 940–950.
[13] M. Corallo, J. Sheridan, M.C. Thompson, Effect of aspect ratio on the near-wake flow structure of an Ahmed body, J. Wind Eng. Ind. Aerodyn. 147 (2015) 95–103.
[14] H. Choi, J. Lee, H. Park, Aerodynamics of heavy vehicles, Annu. Rev. Fluid Mech. 46 (2014) 441–468.
[15] C. Gurlek, B. Sahin, G.M. Ozkan, PIV studies around a bus model, Exp. Therm. Fluid Sci. 38 (2012) 115–126.
[16] T. Han, V. Sumantran, C. Harris, T. Kuzmanov, M. Huebler, T. Zak, Flow-Field Simulations of Three Simplified Vehicle Shapes and Comparison With Experimental Measurements. SAE Paper 1996, 960678.
[17] W. Yi, Drag Reduction of a Three-Dimensional Car Model Using Passive Control Device PhD Thesis, Seoul National University, Korea, 2007.
[18] J. Lee, H. Choi, Large eddy simulation of flow over a three-dimensional model vehicle, in: Proceeding of the 6th International Symposium of Turbulence and Shear Flow Phenomena, 22–24 June, 2009, Seoul, Korea, 2009.

[19] R. Verzicco, M. Fatica, G. Iaccarino, P. Moin, B. Khalighi, Large eddy simulation of a road vehicle with drag-reduction devices, AIAA J. 40 (2002) 2447–2455.
[20] R.H. Croll, W.T. Gutierrez, B. Hassan, J.E. Suazo, A.J. Riggins, Experimental Investigation of the Ground Transportation System (GTS) Project for Heavy Vehicle Drag Reduction, SAE Technical Paper, 1996, Paper No. 960907.
[21] C.J. Roy, J. Payne, M. McWherter-Payne, RANS simulations of a simplified tractor/trailer geometry, J. Fluid Eng. 128 (2006) 1083–1089.
[22] K. Salari, J.M. Ortega, P.J. Castellucci, Computational Prediction of Aerodynamic Forces for a Simplified Integrated Tractor-Trailer geoMetry, AIAA Paper 2004, 2004–2253.
[23] B.L. Storms, D.R. Satran, J.T. Heineck, S.M. Walker, A study of Reynolds Number Effects and Drag-Reduction Concepts on a Generic Tractor-Trailer, AIAA Paper 2004, 2004-2251.
[24] D.G. Hyams, K. Sreenivas, R. Pankajakshan, D.S. Nichols, W.R. Briley, D.L. Whitfield, Computational simulation of model and full scale Class 8 trucks with drag reduction devices, Comput. Fluids 41 (2011) 27–40.
[25] P.J. Castellucci, K. Salari, Computational Simulation of Tractor-Trailer Gap Flow with Drag-Reduction Aerodynamic Devices, SAE Paper 2005, 2005-01-3625.
[26] K.R. Cooper, Truck Aerodynamics Reborn-Lessons from the Past. SAE Technical Paper, 2003, 2003-01-3376.
[27] R.M. Buil, L.C. Herrer, Aerodynamic analysis of a vehicle tanker, J. Fluid Eng. 131 (2009) 0412041–004120417.
[28] R.M. Wood, X.S. Bauer, Simple and Low-Cost Aerodynamic Drag Reduction Devices for Tractor-Trailer Trucks, SAE Technical Paper, 2003, 2003-01-3377.
[29] C.M. Mugnaini, Aerodynamic Drag Reduction of a Tractor-Trailer Using Vortex Generators: a Computational Fluid Dynamic Study Master of Science Thesis, California State University, Sacramento , United States, 2015.
[30] V. Malviya, R. Mishra, J. Fieldhouse, CFD investigation of a novel fuel-saving device for articulated tractor-trailer combinations, Eng. Appl. Comput. Fluid Mech. 3 (2009) 587–607.
[31] L. Taubert, I. Wygnanski, Preliminary experiments applying active flow control to a 1/24th scale model of a semi-trailer truck, Lecture Notes Appl. Comput. Mech. 41 (2009) 105–113.
[32] J. Ortega, K. Salari, B. Storms, Investigation of tractor base bleeding for heavy vehicle aerodynamic drag reduction, in: Proceeding of the International Conference on Aerodynamics of Heavy Vehicles II: Trucks, Buses and Trains, 26–31 August, 2007, Lake Tahoe, California, United States, 2007.
[33] S. Krajnovic, L. Davidson, Numerical study of the flow around a bus-shaped body, ASME J. Fluids Eng. 125 (2003) 500–509.
[34] B. Blocken, Y. Toparlar, T. Andrianne, Aerodynamic benefit for a cyclist by a following motorcycle, J. Wind Eng. Ind. Aerodyn. 155 (2016) 1–10.
[35] J.B. Barlow, R. Guterres, R. Razenbach, Experimental parametric study of rectangular bodies with radiused edges in ground effect, J. Wind Eng. Ind. Aerodyn. 89 (2001) 1291–1309.
[36] Product-Manual of Davis 8.2 Software; Publisher: LaVision GmbH Gottingen, Germany, 2013, pp. 284–299.
[37] K.H. Lo, K. Kontis, Flow characteristics of various three-dimensional rounded contour bumps in a Mach 1.3 freestream, Exp. Therm. Fluid Sci. 80 (2017) 228–243, http://dx.doi.org/10.1016/j.expthermflusci.2016.08.027.
[38] K.H. Lo, H. Zare-Behtash, K. Kontis, Control of flow separation on a contour bump by jets in a Mach 1.9 freestream: an experimental study, Acta Astronautica 126 (2016) 229–242.
[39] W.T. Lusk, Control of Supersonic Cavity Flow by Leading Edge Blowing Master Thesis, University of Florida, United States, 2011.
[40] T. Lusk, J. Dudley, L. Ukeiley, L. Cattafesta, Flow field effects on control on supersonic open cavities, in: Proceedings of 49th AIAA Aerospace Sciences Meeting Including the New Horizons Forum and Aerospace Exposition, Orlando, Florida, United States, 4–7 January, 2011, 2011.
[41] T. Lusk, L. Cattafesta, L. Ukeiley, Leading edge slot blowing on an open cavity in supersonic flow, Exp. Fluid 53 (2012) 187–199.
[42] M. Samimy, S.K. Lele, Motion of particles with inertia in a compressible free shear layer, Phys. Fluids 3 (1991) 1915–1923.